Bulletin of the Seismological Society of America, Vol. 97, No. 4, pp. 1176–1195, August 2007, doi: 10.1785/0120060251

A New Method for Determining Small Earthquake Source Parameters Using Short-Period *P* Waves

by Ying Tan and Don Helmberger

Abstract We developed a new technique of inverting short-period (0.5–2 Hz) *P* waveforms for determining small earthquake (M <3.5) focal mechanisms and moments, where magnitude ~4 events with known source mechanisms are used to calibrate the "unmodeled" structural effect. The calibration is based on a waveform cluster analysis, where we show that clustered events of different sizes, for example, M ~4 versus M ~2, display similar signals in the short-period (SP, 0.5–2 Hz) frequency band, implying propagational stability. Since both M ~4 and M ~2 events have corner frequencies higher than 2 Hz, they can be treated as point sources, and the "unmodeled" structural effect on the SP *P* waves can be derived from the magnitude 4 events with known source mechanisms. Similarly, well-determined magnitude 2's can provide calibration for studying even smaller events at higher frequencies, for example, 2–8 Hz. In particular, we find that the "unmodeled" structural effect on SP *P* waves is mainly an amplitude discrepancy between data and 1D synthetics. The simple function of "amplitude amplification factor" (AAF) defined as the amplitude ratio between data and synthetics provides useful calibration, in that the AAFs derived from different clustered events appear consistent, hence stable and mechanism independent. We take a grid-search approach to determine source mechanisms by minimizing the misfit error between corrected data and synthetics of SP *P* waves. The validation tests with calibration events demonstrate the importance and usefulness of the AAF corrections in recovering reliable results. We introduce the method with the 2003 Big Bear sequence. However, it applies equally well to other source regions in southern California, because we have shown that the mechanism independence and stability of the AAFs for source regions of 10 km by 10 km are typical. By definition, the AAFs contain the effects from the station site, the path, and crustal scattering. Although isolating their contributions proves difficult, the mechanism independence and stability of the AAFs suggest that they are mainly controlled by the near-receiver structure. Moreover, the ratios between the AAFs for the vertical and radial components from various events at different locations appear consistent, suggesting that these AAF(v)/AAF(r) ratios might be simple functions of site conditions. In this study, we obtained the focal mechanisms and moments for 92 Big Bear events with M_L down to 2.0. The focal planes correlate well with the seismicity patterns, while containing abundant finer-scale fault complexity. We find a linear relationship between $\log(M_0)$ and M_L, that is, $\log(M_0) = 1.12M_L + 17.29$, which explains all the data points spanning three orders of magnitude ($2.0 < M_L < 5.5$).

Introduction

The focal mechanisms of small earthquakes (M <4) are commonly used to infer fault structure (e.g., Shearer, 1998), to constrain stress field (e.g., Hauksson, 1994; Hardebeck and Hauksson, 2001), and to test stress-triggering hypotheses (e.g., Beroza and Zoback, 1993; Kilb *et al.*, 1997). Their uncertainties, however, often weaken the robustness of the results. Therefore, it is important to determine small earthquake focal mechanisms as accurately as possible.

The most widely used method for determining small earthquake focal mechanisms is to construct focal plots from first-motion polarities (e.g., FPFIT by Reasenberg and Oppenheimer, 1985; Hardebeck and Shearer, 2002). Since only

the binary up or down of the first motions counts in these methods, a dense sampling of the focal sphere is required to form a reliable solution. For many small earthquakes, the lack of sufficient first-motion observations causes large uncertainties in their focal mechanisms.

With the widespread growth of broadband instruments, long-period (>5 sec) waveform inversion techniques have been developed and proven effective in retrieving accurate source mechanisms of earthquakes with $M \sim 3.5$ and greater (e.g., Zhu and Helmberger, 1996; Liu *et al.*, 2004). Since seismic waveforms contain much more information about the source than the first-motion polarities alone, even sparse data sets suffice for the task (e.g., Tan *et al.*, 2006). The same strategy, however, can hardly be applied to smaller events, because of the poor signal-to-noise ratios (SNRs) (see Fig. 1). These small events have to be analyzed at much higher frequencies (e.g., >0.5 Hz).

Although adequate velocity models are not yet developed to practically reproduce the complete short-period records, the direct *P* and *S* arrivals are relatively simple and useful for constraining source mechanisms. For example, adding *P*- and/or *S*-wave amplitude information can remedy the scarcity of first-motion polarities on a focal sphere, if corrections are made for event magnitude, geometrical spreading, attenuation, and station site effect. In the seismic literature of the past two decades, studies of using absolute *P*- and *S*-wave amplitudes (e.g., Ebel and Bonjer, 1990; Nakamura *et al.*, 1999) or their relative amplitude ratios (e.g., Kisslinger, 1980; Natale *et al.*, 1991; Schwartz, 1995; Julian and Foulger, 1996; Rau *et al.*, 1996; Hardebeck and Shearer, 2003) for determining earthquake source mechanisms were fairly common. Despite the detailed differences in the approaches of these investigations, their conclusions are mixed regarding whether and how much adding amplitude data can improve the focal mechanisms from first-motion polarities. For example, although Rau *et al.* (1996) and Natale *et al.* (1991) showed large uncertainty reduction in the fault parameters with the inclusion of *S*/*P*-amplitude ratios, the work of Hardebeck and Shearer (2003) raised some concern. Hardebeck and Shearer (2003) reported considerable "noise" in the observed *S*/*P* ratios from "similar" event clusters in the Northridge and Anza regions. California, which limited the usefulness of the *S*/*P* ratios in determining focal mechanisms. Ebel and Bonjer (1990) used both *P*- and *S*-wave amplitudes to determine focal mechanisms of six events in Germany. They showed that the amplitude data were strongly controlled by the earthquake radiation patterns, and their solutions agreed well with those determined from a large number of first-motion polarities. However, Nakamura *et al.* (1999) reported poor amplitude misfit reduction, although they could obtain a large set of spatially coherent focal mechanisms in Japan using absolute *P*- and *S*-wave amplitudes.

Such discrepancies are largely due to unmodeled short-wavelength crustal heterogeneities. Several studies have emphasized the importance of velocity models in using *P*- and/or *S*-wave amplitude data for source mechanism determination (e.g., Saikia and Herrmann, 1985; Ebel, 1989; Ebel and Bonjer, 1990; Sileny *et al.*, 1992). In particular, the details of the near-receiver structure can easily disturb the observed amplitudes. Moreover, the early coda waves generated by scatters can be confused with the direct arrivals, especially near the nodal planes. Thus, the focal mechanisms obtained by simply matching the amplitude data with an inadequate velocity model may be erroneous. Because high-resolution velocity models are usually not available, it is worthwhile to develop techniques that use empirical path corrections.

Here we introduce such a method that uses calibrated short-period (0.5–2 Hz) *P* waves to determine small earthquake focal mechanisms and moments. We focus on the direct *P* arrivals, because the *S* waves are apparently more complicated due to *P*-to-*SV* or *SV*-to-*P* conversions (Ebel, 1989). Moreover, rather than fitting amplitude measurements, we intend to match the *P* waveforms. A few previous attempts have been made to invert high-frequency *P* and/or *S* waveforms for determining earthquake source mechanisms (e.g., Saikia and Herrmann, 1986; Koch, 1991a,b; Schurr and Nábělek, 1999); however, because all these studies were restricted to very close observations (epicentral distance ≤ depth) to justify the use of simple crustal models, their applications are limited.

In this study, we use available *P* waveform data at all distances up to ~200 km and correct the "unmodeled" propagational contaminations by analyzing clustered events of different sizes. The feasibility of such a waveform cluster analysis is displayed in Figure 1, where we compare the vertical records at the same station (GSC) from three events of different sizes (M_L 4.61 versus 2.41 versus 1.78). These events are all from the 2003 Big Bear sequence and located within ~500 m of one another (Chi and Hauksson, 2006). The records from the two smaller events (13937632 and 13939108) are dominated by noise in the long-period (LP, 5–50 sec) frequency band. However, at shorter periods, for example, 0.5–2 Hz, the magnitude 2 event (13937632) displays very similar wave trains as the magnitude ~4 event (13938812). This implies propagational stability along the path, although how much of the complexity is caused by the entire path versus locally near the station site is not well known. Also note that both events have corner frequencies higher than 2 Hz and hence can be treated as point sources. Therefore, if the "unmodeled" structural effect on the short-period (SP, 0.5–2 Hz) *P* waves can be derived from the magnitude 4 event (13938812), it can be corrected for determining the source mechanism of the magnitude 2 event (13937632). The same strategy also applies to higher frequencies, for example, 2–8 Hz, where well-determined magnitude 2 events can provide excellent calibrators (Fig. 1). In the following, we will focus on the SP band, 0.5–2 Hz, for the details of the path calibration and source inversion, and some results for 2–8 Hz will be given in the discussion. In particular, we show that short-period *P* waves (0.5–2 Hz)

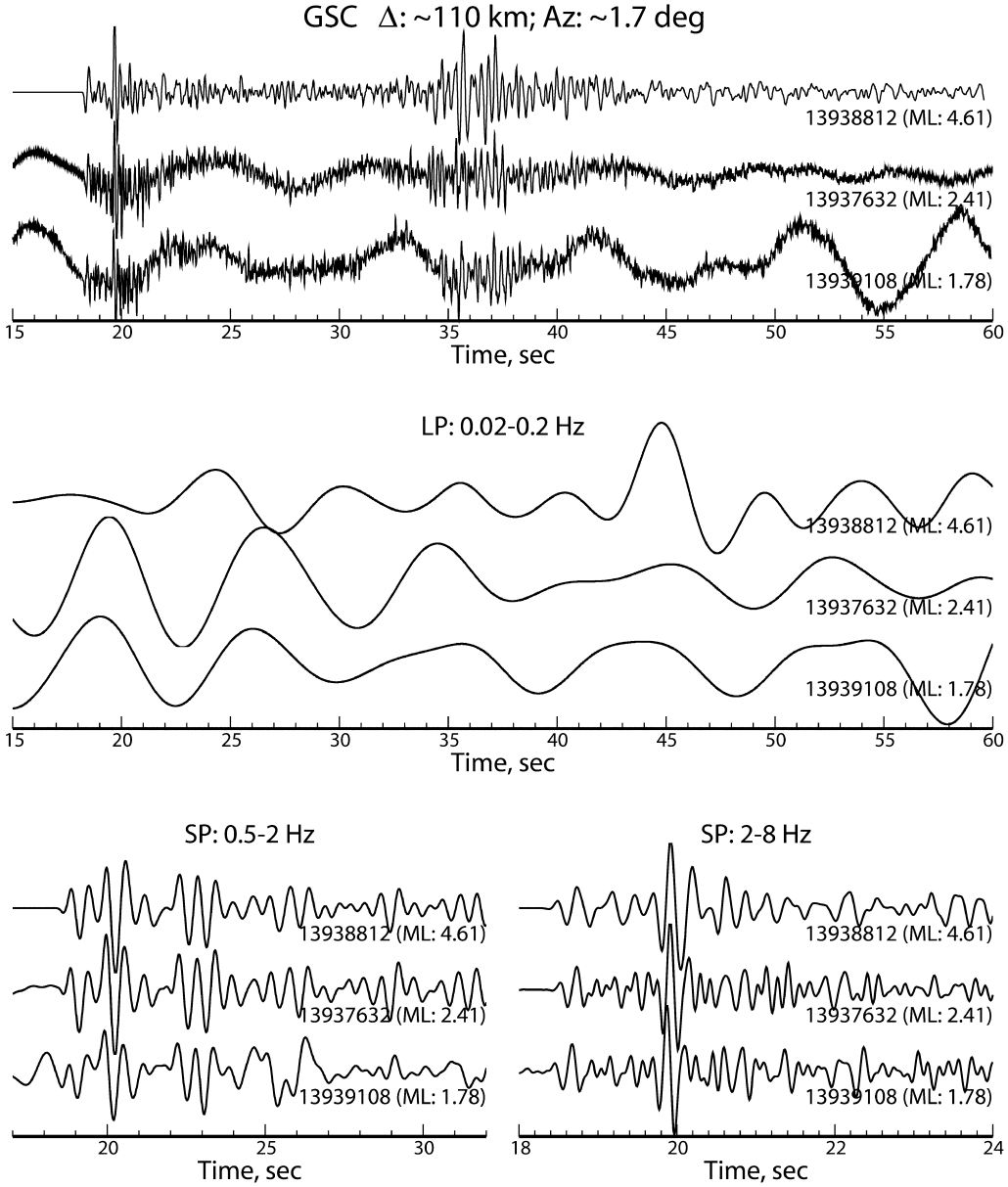

Figure 1. The comparison of the GSC records of three clustered, but different-sized events from the 2003 Big Bear sequence. The original broadband and filtered records of different frequency bands (0.02–0.2 Hz, 0.5–2 Hz, 2–8 Hz) are displayed from top to bottom. In particular, the short-period (SP) comparisons are concentrated on the *P*-wave trains.

can be reasonably well explained by a simple 1D model, provided that station-specific "amplitude amplification factor" (AAF) corrections are applied. By inverting these *P*-wave waveforms, accurate source mechanisms of events with M_L down to ~2.0 can be obtained. We demonstrate the method with the 2003 Big Bear sequence (see Fig. 2), because this cluster contains several events with well-determined long-period solutions, ideal for calibration. Further, the cluster occurred in the center of the southern California (SC) TriNet array, and in general was well recorded. However, as displayed in Figure 2, many interesting seismic zones are scattered throughout SC, a few of which will be addressed in the discussion section.

Short-Period *P*-Wave Calibration

The idea of using magnitude 4 events with known source parameters to calibrate regional paths was introduced previously by Song and Helmberger (1998), where they build pseudo Green's functions by perturbing individual generalized ray responses from a 1D model. Here we restrict our attention to short-period (0.5–2 Hz) direct *P* waves, be-

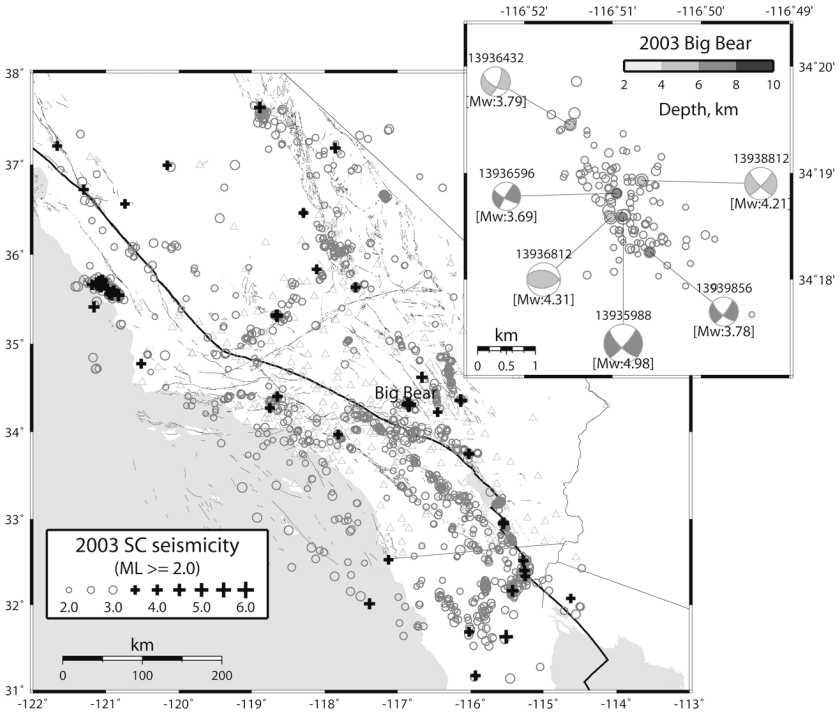

Figure 2. Southern California earthquakes in 2003 (circles and crosses) along with the broadband TriNet stations (triangles). An enlarged Big Bear region is included with the mechanisms of events larger than M_w >3.5.

cause we plan to use these *P* waves (mainly P_g and P_n phases) for determining source mechanisms of smaller events. Moreover, they are the parts of the seismograms that are most easily isolated and understood in terms of crustal complexity. For example, we compare in Figure 3 the observed *P* waves (black) and the synthetics (red) for a strike-slip event (13938812), where a waveform cross-correlation technique has been applied to align them. To avoid the waveform complexities that are not easily explained at some stations, we simply discard them and concentrate on the high-quality fits with cross-correlation values higher than 90. This resulted in a loss of about one-third of the recording stations, but we still have good azimuthal coverage. A smoothed version of the SoCal (SC) model (Fig. 4) is used to calculate the synthetics with a reflectivity code (Zhu and Rivera, 2002) to simplify the high-frequency triplications associated with the layered boundaries. This smoothed SC model does produce an overall better fit to the observations. However, at long periods (e.g., >5 sec), the differences between the synthetics from the two models are hardly discernible. For simplicity, a 0.2-sec triangular source time function has been assumed, which fits the observed *P*-wave waveforms at most stations.

The discrepancies between the observed *P* waves and the synthetics in Figure 3 are mainly manifested as amplitude differences, which we can readily quantify with the function of AAF defined as

$$\mathrm{AAF} = \sqrt{\frac{\int u^2(t)dt}{\int s^2(t)dt}}. \qquad (1)$$

Here $u(t)$ and $s(t)$ are the data and synthetics, respectively, and the integrations are performed on ~2-sec windows centered on the first *P* arrivals. It appears in Figure 3 that the most anomalous AAFs occur at stations in the extended Los Angeles Basin. In particular these stations are consistently characterized by large AAFs (>1) on the vertical component, but small AAFs (<1) on the radial component. This discrepancy between the vertical and radial components has been noted by many previous investigators (e.g., Savage and Helmberger, 2004). They attributed it to a low-velocity layer beneath the stations that bends the rays to be nearly vertical approaching the surface, hence greatly reducing the *P*-wave strength on the radial component. The radial component *P* waves also tend to become broader and arrive later than their vertical-component counterparts. In fact, such features are widely observed at most stations, even some "hard rock" sites, for example, RRX and GSC, and the *P*-wave radiation pattern unfortunately is blurred with the laterally varying AAFs. Therefore, these amplitude distortions have to be appropriately corrected before we can use the short-period *P* waves for determining source mechanisms.

To account for the AAFs by refining velocity models proves difficult, simply because of our poor knowledge of their origins. However, the fact that the AAFs derived from different events appear consistent suggests that the AAFs themselves provide good calibration. This inference is based on the comparisons among the AAFs derived from the eight clustered calibration events (see Fig. 5). Except for the five events from the 2003 Big Bear sequence, the three events (9069997: 1998/10/27, 01:08:40.6; 9070083: 1998/10/27, 15:40:17.1; 9105672: 1999/09/20, 07:02:49.2) that occurred within the cluster in the past with known source mechanisms

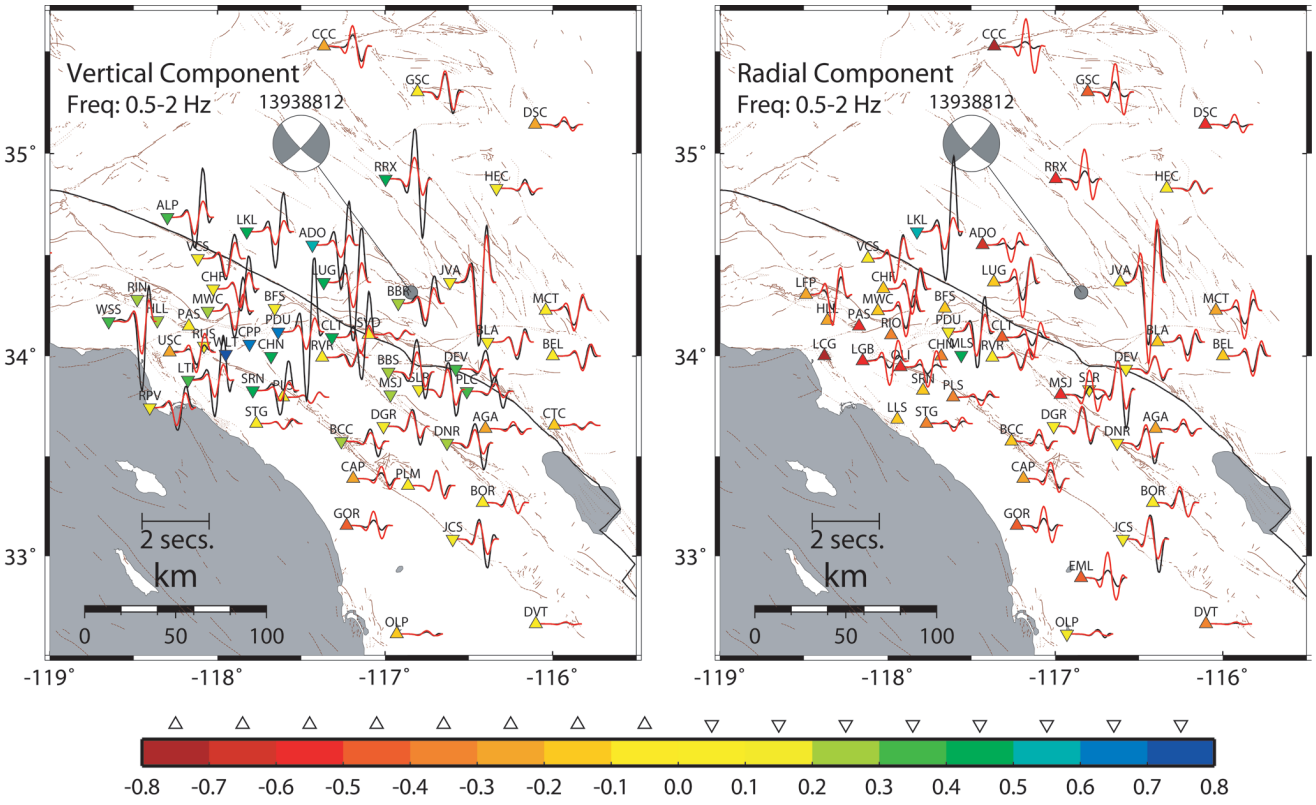

Figure 3. *P*-wave waveform comparison between the data (black) and synthetics (red) for a strike-slip event (13938812) on the vertical (left) and radial (right) components. Only the stations that have waveform cross-correlation values larger than 90 are shown. The traces for some stations in the crowded Los Angeles Basin are removed for display purposes. The stations are color coded according to their log(AAF) values, where a triangle indicates a negative value and an inverse triangle indicates a positive one.

are also included. Note that we have discarded the mainshock (13935988) in Figure 5 because of the source complexity that cannot be ignored at 0.5–2 Hz as discussed in Tan (2006). A detailed example of such comparisons is displayed in Figure A1 of Appendix A, between the AAFs derived from the strike-slip event (13938812) and the distinctly different thrust event (13936812).

Here we summarize these comparisons by calculating the averages and deviations of the AAFs derived from the calibration events (Fig. 6). In this case,

$$\overline{\log(\mathrm{AAF})} = \frac{1}{N}\sum_{i=1}^{N}\log(\mathrm{AAF}_i) \qquad (2)$$

$$s^2_{\log(\mathrm{AAF})} = \frac{1}{N-1}\sum_{i=1}^{N}\left(\log(\mathrm{AAF}_i) - \overline{\log(\mathrm{AAF})}\right)^2. \qquad (3)$$

Only the stations that have AAF estimates associated with high-quality fits (cc $\geq$90) from at least three events are shown in Figure 6. Nearly all the stations display reasonably small deviations ($s_{\log(\mathrm{AAF})} < 0.20$), suggesting that the AAFs can provide practically useful station-specific corrections for the propagational effect on the short-period (0.5–2 Hz) *P* waves. The larger deviations observed at the couple of stations, such as THX and HEC, might imply more complicated local structure beneath the sites. In fact, besides fine-scale structural heterogeneities, small errors in the events locations and mechanisms, as well as their rupture directivity effects, can also cause scatters or perhaps biases in the AAF estimates. Recently, Chen *et al.* (2005) demonstrated an example of using the *P*-wave amplitude signals in the 0.5–2.5 Hz frequency band to solve for rupture directivity of a M_w 4.3 event. However, as we have found in another study (Tan and Helmberger, manuscript in preparation), only a couple of the calibration events that are used here display consistent and significant azimuthal variations in the apparent source durations; hence, the source effects of these calibration events are more likely to cause scatters in the AAF estimates rather than systematically bias them.

Short-Period *P*-Wave Inversion

Because the process is highly nonlinear, we take a grid-search approach similar to that used in the long-period in-

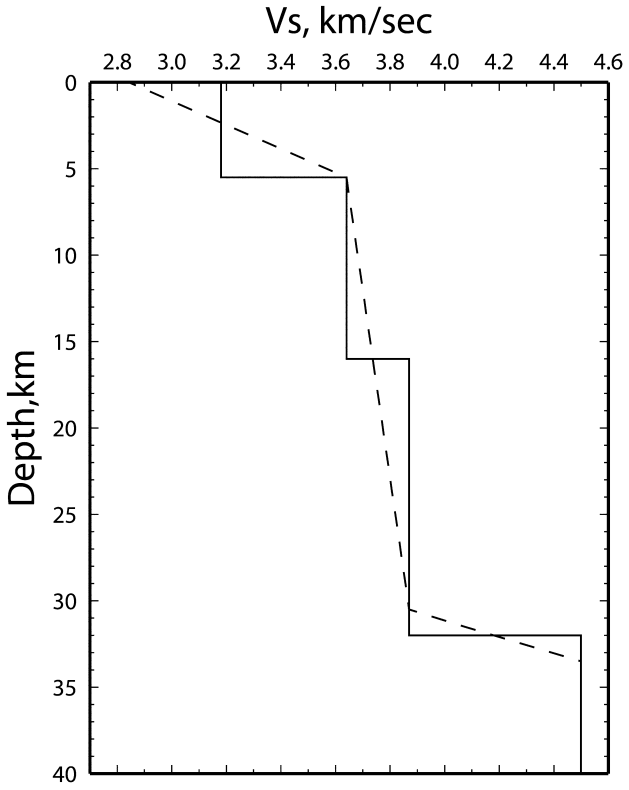

Figure 4. Comparison of the layered SoCal (SC) model from Dreger and Helmberger (1993) (solid line) and the smoothed one (dashed line) used in this study.

versions (e.g., Zhao and Helmberger, 1994; Zhu and Helmberger, 1996) to invert short-period (0.5–2 Hz) *P* waves for determining focal mechanisms and moments. We minimize the L_2 norm of the misfit between the corrected data and synthetics:

$$e = \|u(t)/\mathrm{AAF} - s(t)\|, \tag{4}$$

where the synthetics of a double-couple source are constructed from the prestored Green's functions of three fundamental faults, namely, vertical strike slip, vertical dip slip, and 45° dip slip (Helmberger, 1983). A reflectivity code (Zhu and Rivera, 2002) has been used for generating these Green's functions with a 1-km interval in both depth and distance. The AAFs in equation (4) are taken from Figure 6 to correct for the amplitude distortions. Moreover, to account for the "unmodeled" timing effect, we allow the synthetics to shift. These shifts determined by waveform cross-correlation during the inversion can be used to refine the starting velocity model as more of them from crossover paths become available.

Validation

As a validation test, we first apply the approach to the eight calibration events (Fig. 5a) with the known focal mechanisms from long-period inversions. This is also the best check of how well the *P*-wave waveforms can constrain focal mechanisms.

For each event, only the stations that show stable AAFs ($s_{\log(\mathrm{AAF})} < 0.20$) in Figure 6 are utilized. Moreover, to avoid possible upgoing and downgoing phase interference at the

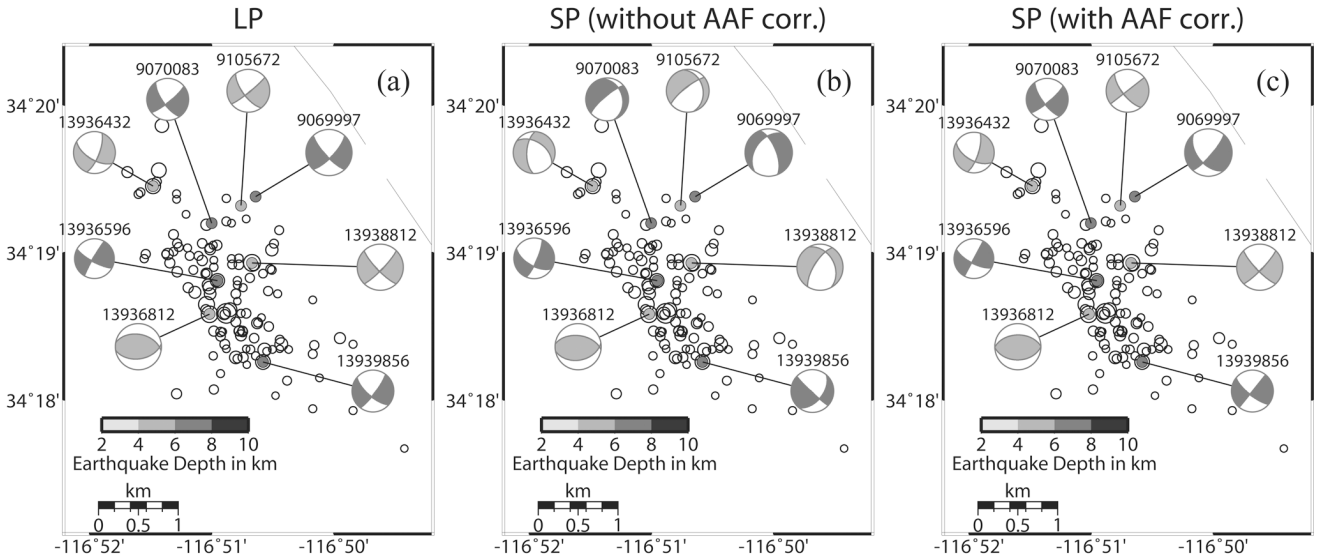

Figure 5. Comparison of focal mechanisms derived from complete long-period (LP) waveform inversions (including both *Pnl* and surface waves) (a), short-period (SP) *P*-wave inversions without the AAF corrections (b), and short-period *P*-wave inversions with the AAF corrections (c). Note the remarkable agreement between (a) and (c).

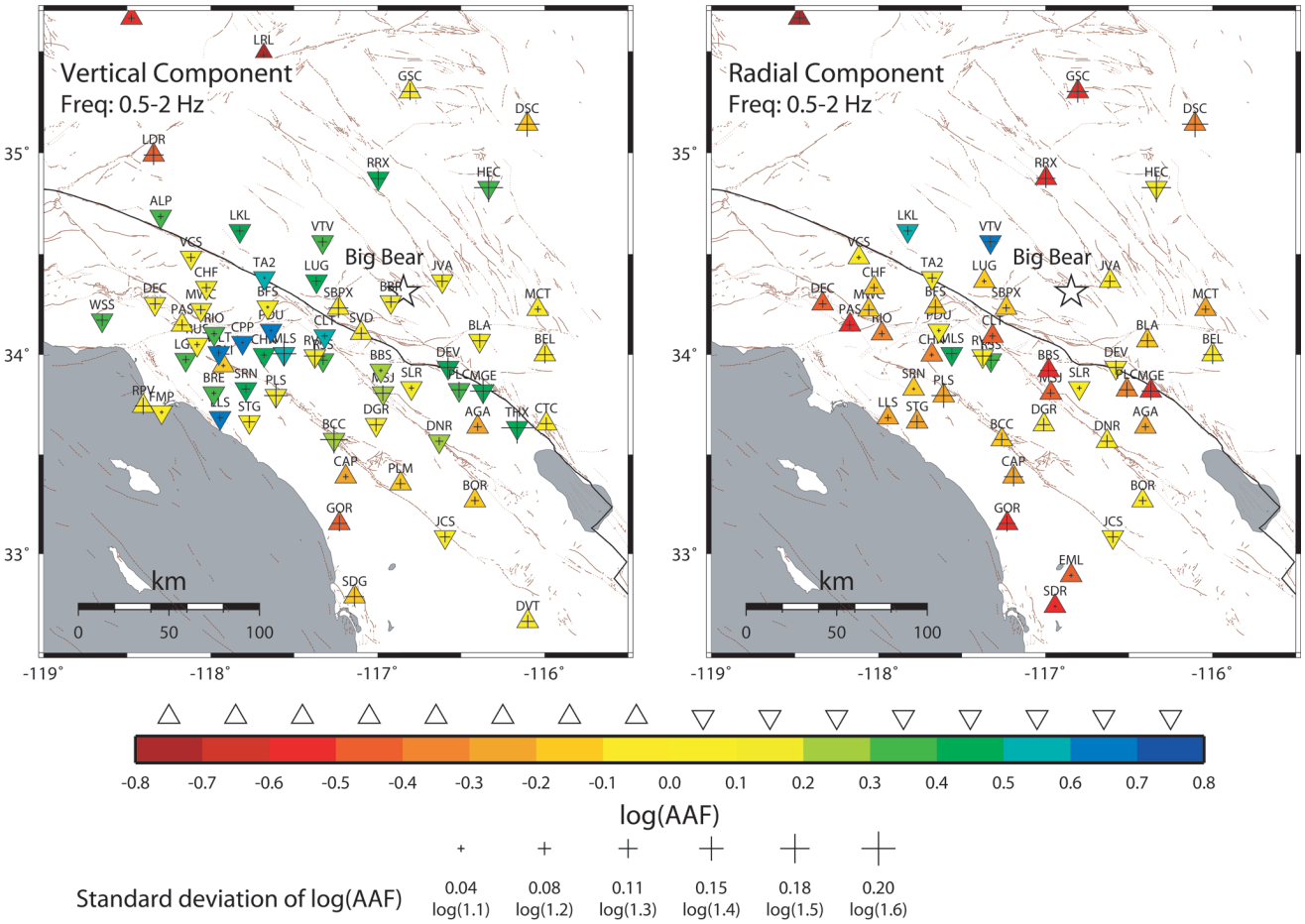

Figure 6. The averaged AAFs for the vertical (left) and radial (right) components derived from the eight calibration events along with the standard deviations (crosses). The negative log(AAF) values are displayed as triangles, and the inverse triangles indicate positive log(AAF) values.

crossover distance (~150 km), we also discarded the few stations with $130 < \Delta < 170$ km. We use the *P*-wave waveforms from both the vertical and radical components, although they basically carry the same constraints. The depths of the events are set at their long-period solutions. However, almost the same focal mechanisms are obtained when we move the events up or down by a couple of kilometers due to the poor sensitivity of *P* waves to event depth. The inversion results show remarkable agreement with the events' known mechanisms (Fig. 5). In particular, the small variations in the focal mechanisms of the strike-slip events are accurately recovered.

To demonstrate the importance of the AAF corrections in equation (4), we also conducted the inversions without them using the same stations (Fig. 5b). The moments of the events are slightly biased, because the log(AAF)s have nearly the opposite signs on the vertical and radial components (Fig. 6) on average. However, although the thrust event remains a thrust, there are significant differences in the solutions of the strike-slip events compared with Figure 5a. Moreover, the inversions with the AAF corrections produce significantly reduced uncertainty estimates of the resolved fault parameters (e.g., Fig. 7. event 13936432).

Random Test with Subsets of Data

We have demonstrated the effectiveness of using the *P*-wave waveforms in constraining focal mechanisms. However, a more important question exists: what is the minimum number of stations that are needed to ensure an accurate mechanism? The station coverage in general gets poorer as an event becomes smaller, and it is for these smaller events that improvements on focal mechanism determination are most needed. Therefore, before we routinely apply the approach to the smaller events of the cluster, we simulate the situation of expected poorer station coverages by using data from only subsets of stations for the calibration events. Four such tests for event 13936432 are shown in Figure 8. In each test, 500 samples of randomly chosen stations of a certain number are used to constrain the event's focal mechanism, and the resulting *P* and *T* axes are compared with the known values. When only five stations are used, where the primary

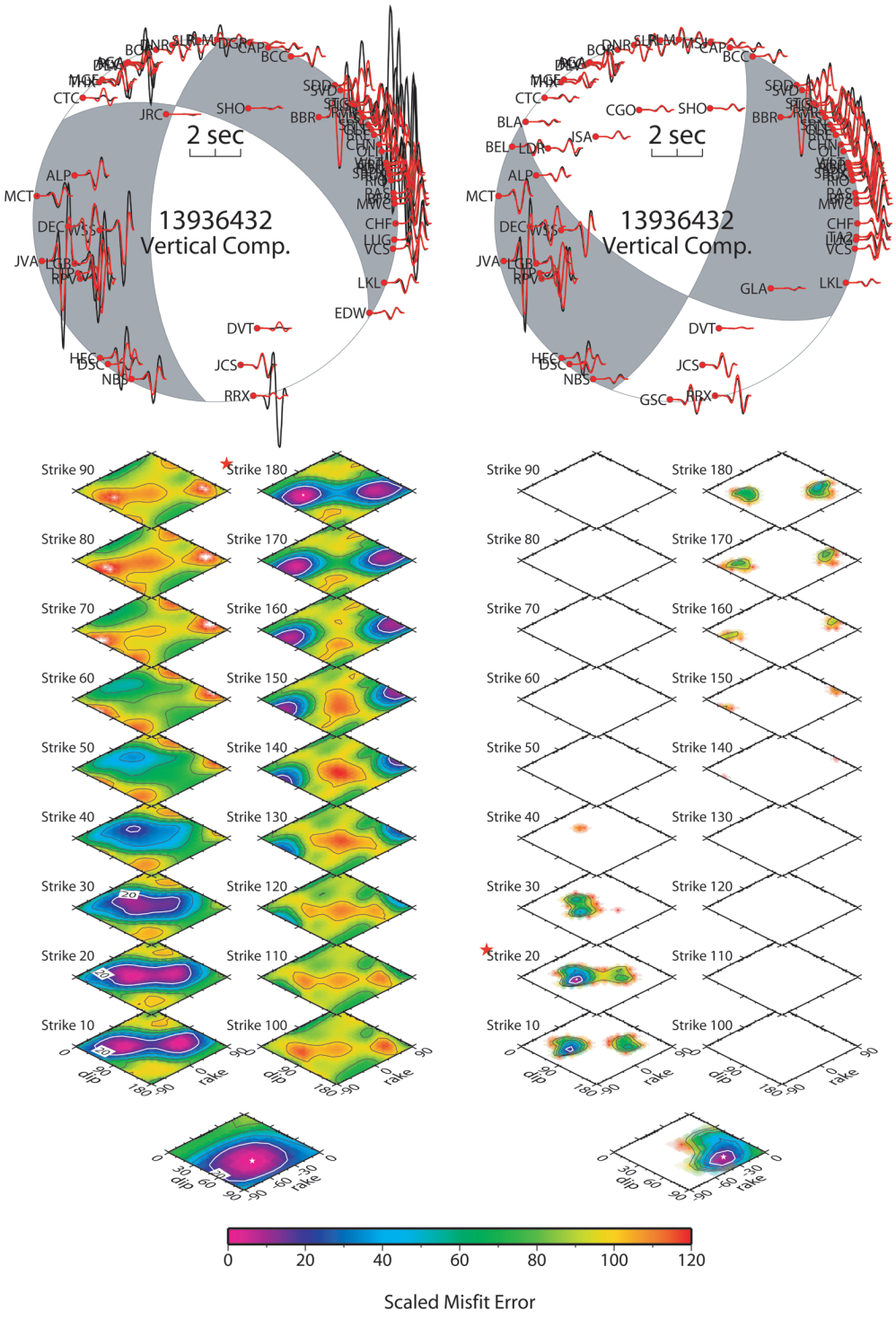

Figure 7. (top) The resulting *P*-wave waveform fits on the vertical component from the short-period inversions without (left) and with AAF corrections (right) for the event 13936432. (bottom) The resolution of the solutions is displayed as the scaled waveform misfit errors. A star indicates where the best solution resides with the blowup of the slice at the bottom. The white contours of 20% variance increase are displayed as the uncertainty estimates.

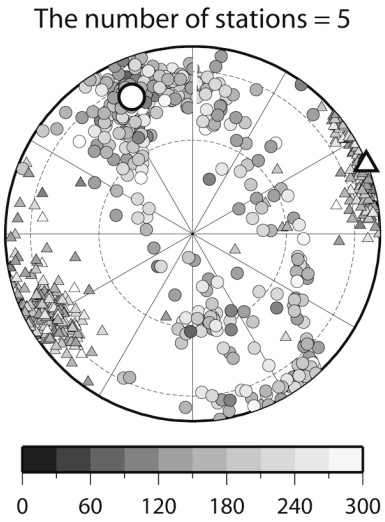

The largest azimuthal gap

	$\Delta\varphi \leq 90°$	$\Delta\varphi \leq 120°$	$\Delta\varphi \leq 360°$
P < 10°	0/2	14/33	191/500
P < 15°	1/2	19/33	247/500
T < 10°	0/2	8/33	121/500
T < 15°	0/2	12/33	196/500

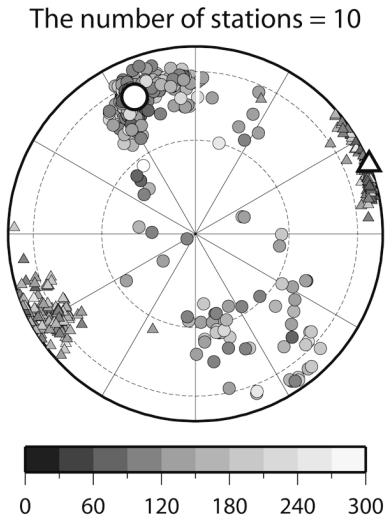

The largest azimuthal gap

	$\Delta\varphi \leq 90°$	$\Delta\varphi \leq 120°$	$\Delta\varphi \leq 360°$
P < 10°	46/53	160/200	350/500
P < 15°	48/53	170/200	392/500
T < 10°	30/53	110/200	229/500
T < 15°	41/53	143/200	319/500

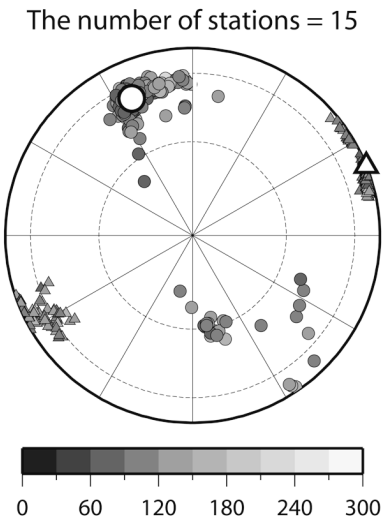

The largest azimuthal gap

	$\Delta\varphi \leq 90°$	$\Delta\varphi \leq 120°$	$\Delta\varphi \leq 360°$
P < 10°	132/141	293/327	431/500
P < 15°	134/141	300/327	451/500
T < 10°	102/141	222/327	324/500
T < 15°	139/141	306/327	440/500

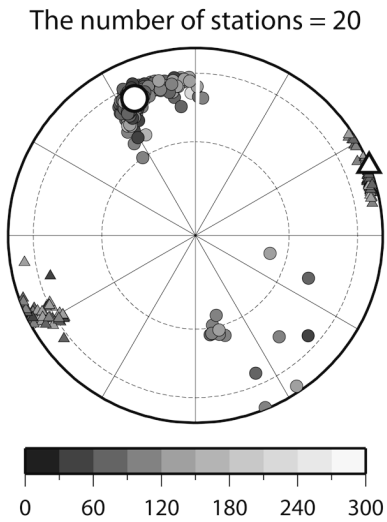

The largest azimuthal gap

	$\Delta\varphi \leq 90°$	$\Delta\varphi \leq 120°$	$\Delta\varphi \leq 360°$
P < 10°	237/251	378/408	446/500
P < 15°	244/251	388/408	469/500
T < 10°	202/251	307/408	363/500
T < 15°	242/251	387/408	454/500

Figure 8. The four panels of this figure display the comparison between the obtained *P* (circles) and *T* axes (triangles) with the known values (open symbols) for event 13936432, when we randomly chose a certain number of stations in the inversion. The detailed results for each case are summarized in the underlying tables, where the fractions of the solutions with certain accuracy for the *P* and *T* axes are given for three respective groups, the largest azimuthal gap $\Delta\varphi \leq 90°$, $\Delta\varphi \leq 120°$, and $\Delta\varphi \leq 360°$. For example, "14/33" in the upper-left table indicates that of 500 random tests, 33 have $\Delta\varphi \leq 120°$, and among them, 14 have the obtained *P* axis deviating from the known value within 10°.

azimuthal gaps in general are larger than 150°, severe scatter occurs in the estimated *P* and *T* axes. However, significant improvements are observed with the addition of more stations. As the number of stations increases to 10, the obtained *P* and *T* axes become more clustered. In particular, about 80% of the *P* axes are within 15° of the known value, whereas the *T* axes show slightly more scatter with more than 60% within 15° of the known value. Furthermore, fifteen or more stations are used, uncertainties of the obtained *P* and *T* axes can be taken as 15° with ~90% confidence. Similar conclusions are reached with the other events. These tests provide a benchmark to assess the accuracy of the focal mechanisms when we apply the approach to the smaller events. However, they might represent a raised threshold of the minimum number of stations that are indeed required, because the available stations are unevenly distributed azimuthally (see Fig. 6).

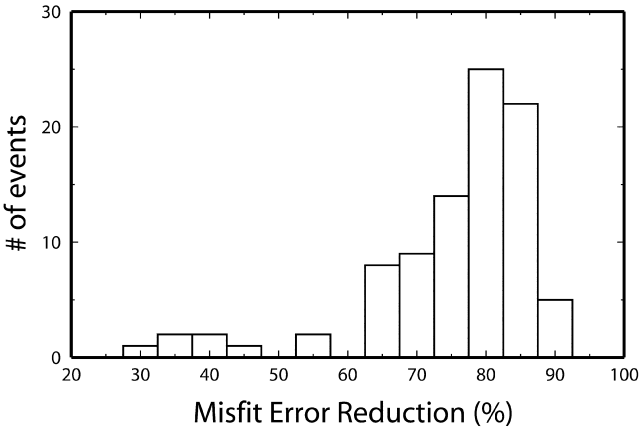

Figure 9. Histogram of the misfit error reduction of the 0.5–2 Hz *P*-wave inversions withAAF corrections from those without AAF corrections for the 2003 Big Bear sequence.

Results

We apply the approach to the smaller events with M_L down to 2.0 within the cluster. The magnitude threshold is chosen to ensure adequate SNR in the selected frequency band (0.5–2 Hz). We use the event depths determined by Chi and Hauksson (2006) plus a +1-km static correction, because their depths for the calibration events are consistently shallower by ~1 km than those determined from long-period waveform inversions. This discrepancy is mainly due to the different velocity models used in the two studies. However, it produces a nearly invisible effect on the resolved focal mechanism solutions. We use the constant AAFs from Figure 6 for the whole sequence, which has been justified by the fact that the AAFs derived from the calibration events appear stable and mechanism independent. However, when we compare the misfit errors as defined in equation (4) from the inversions with and without the AAF correction (Fig. 9), the uniformly large misfit error reduction for all the events confirms the appropriateness of the AAFs.

Figure 10 displays the focal mechanisms of 83 events, together with the long-period solutions of nine bigger ones (including the mainshock). We consider the uncertainties of the strike, dip, and rake angles of these solutions to be within 15° with 90% confidence, because these are the events with either more than 15 stations effectively used in the inversion or more than 10 stations with the largest azimuthal gap $\Delta\varphi \leq 90°$. Such a restriction disqualifies about 20 events (the open circles in Fig. 10), where most of them are contaminated by the coda of other events.

In Figure 10 it appears that the whole sequence is dominated by strike-slip events. There are thrust and normal events, but they only occupy a small percentage. This overall pattern of source mechanisms is consistent with earlier reports in this region (e.g., Hauksson *et al.*, 1993). We plot the events at the locations refined by Chi and Hauksson (2006) with a double-difference approach. The clear northwest-trending swath of seismicity is probably associated with the mainshock (13935988) rupture. However, the seismicity does not collapse onto a single fault; there are multiple fault segments (Chi and Hauksson, 2006). There is, in general, good correlation between the seismicity patterns and focal planes. In particular, most of the deeper events (>6.0 km) to the south show northwest-striking nodal planes consistent with the seismicity trend, which might indicate that the ruptures are probably along a single fault zone. In contrast, the shallower events to the north display larger variations in the focal mechanisms, quite a few events have nodal planes that depart significantly from the general northwest trend. Another small, but interesting feature in Figure 10 is the "sharp rotation" of fault plane, such as implied by the two events 13936416, and 13943624 highlighted. These two events are located almost at the same spot, but their focal mechanisms clearly show a ~30° difference in strike of the fault plane, which is reliably recovered by the waveform inversion (see Fig. 11). Note the obviously different *P*-wave radiation patterns for the two events. In addition, polarity reversals are observed at a few stations, such as HEC, SVD, and BBR. This kind of change in fault-plane geometry might suggest a newly developing fault system.

Seismic Moment (M_0) versus M_L

Although they are both measures of earthquake size, M_0 and M_L are fundamentally different. Basically, M_0 is based on a well-accepted shear dislocation source model and can be estimated from all suitable seismic records, whereas M_L is derived from specific instrumental measurements and not easily related to the physical characteristics of the earthquake source. However, because M_L has been widely used and is more readily available, empirical relationships between M_0 and M_L have been common in seismological literature (e.g., Hanks and Boore, 1984; Vidal and Mungúia, 1991; Abercrombie, 1995; Thio and Kanamori, 1995, Ben-Zion and

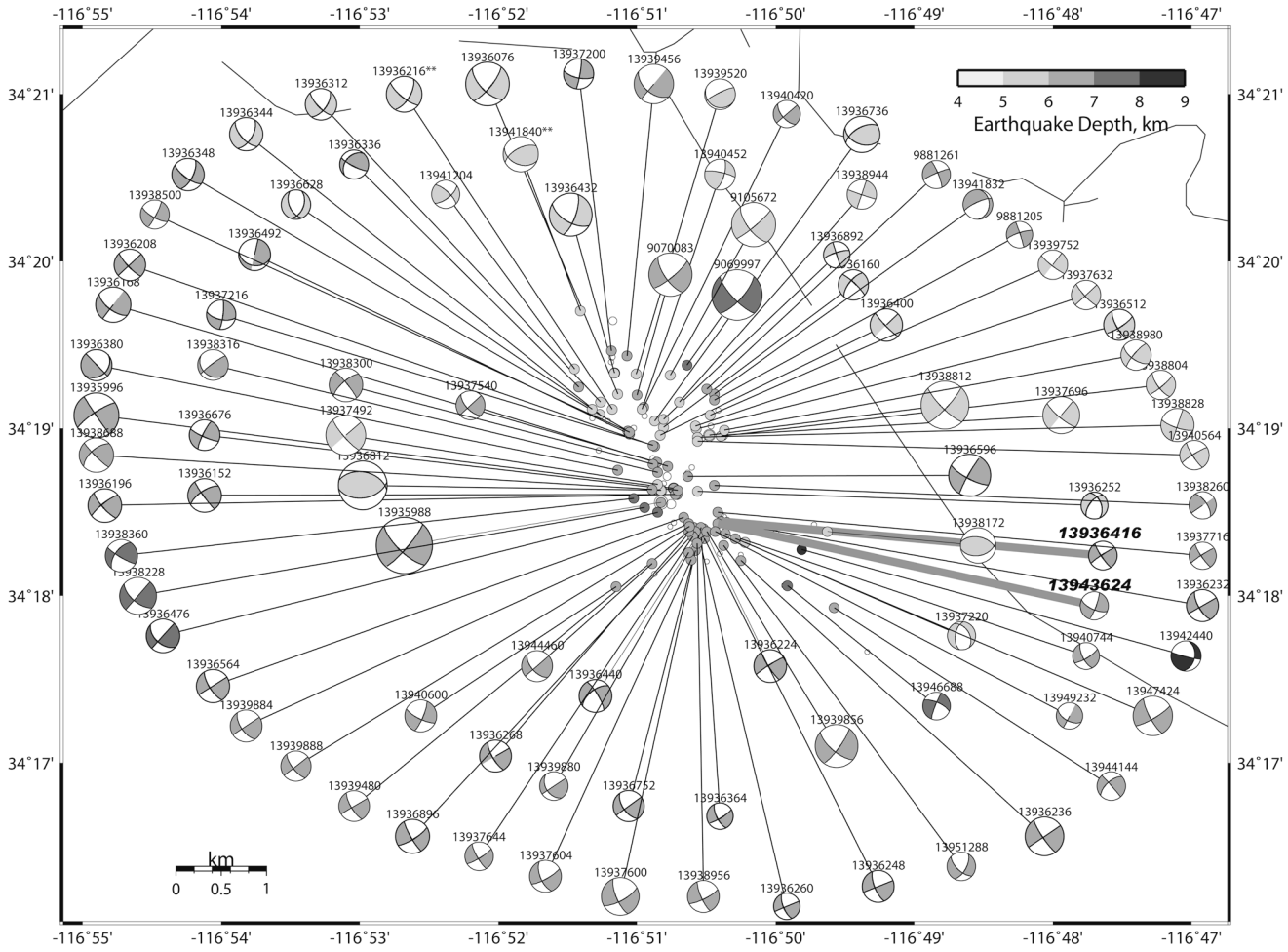

Figure 10. Map containing 92 events with mechanisms and moments (size of beach balls). The event locations are from Chi and Hauksson (2006) with a double-difference approach. Note the general northwest–southeast trend of seismicity, consistent with the mainshock rupture. The two events (13936416 and 13943624) highlighted will be compared in Figure 11.

Zhu, 2002; Clinton *et al.*, 2006), which has provided useful calibration between M_L and M_0 for earthquake source studies (e.g., Hardebeck and Hauksson, 1997) as well as seismic-hazard analysis (e.g., Atkinson and McCartney, 2005; Braunmiller *et al.*, 2005). These empirical relations also suggest that the scaling between $\log(M_0)$ and M_L varies with earthquake size, although the complete pattern, origin, or implication of such variations remain inconclusive. In particular, Hanks and Boore (1984) presented theoretical evidence for the continuous curvature of $\log(M_0)$ versus M_L based on their stochastic simulations of high-frequency ground motions (Boore, 1983). They attributed the nonlinear scaling factor between $\log(M_0)$ and M_L to a complex interaction in the frequency domain among the natural frequency of the standard Wood–Anderson torsion seismograph (f_s), the earthquake corner frequency (f_0), and the path-dependent high-frequency cutoff (f_m), which results in the significant departure from the usually assumed or theoretically expected $\log(M_0) \propto 1.5M_L$ relationship for both large ($f_0 \leq f_s$) and small ($f_0 > f_m$) events. Later work by Ben-Zion and Zhu (2002) suggested a possible alternative explanation of the nonlinearity in the scaling between $\log(P_0)(P_0 = M_0/\mu)$ and M_L from their simulated earthquake patterns (e.g., Ben-Zion and Rice, 1993). They showed the transition between the limiting scaling regimes, whether sharp or gradual, can be indicative of the stress-field evolution. More recently, Deichmann (2006) revisited the problem and demonstrated that the systematic deviations of the $\log(M_0) - M_L$ scaling from $\log(M_0) \propto 1.5M_L$ contain useful information about physical properties of the earthquake source or the "unmodeled" propagational effect, especially the attenuation effect in measuring M_L. It appears that to clarify the true variations in the scaling between $\log(M_0)$ and M_L, their implications require more observations, in particular for small events ($M < 4$) where good M_0 estimates are generally lacking.

Here we display the $\log(M_0)$ versus M_L relation for the 92 events ($2.0 < M_L < 5.5$) within the 2003 Big Bear sequence that we have studied (Fig. 12a), where the large num-

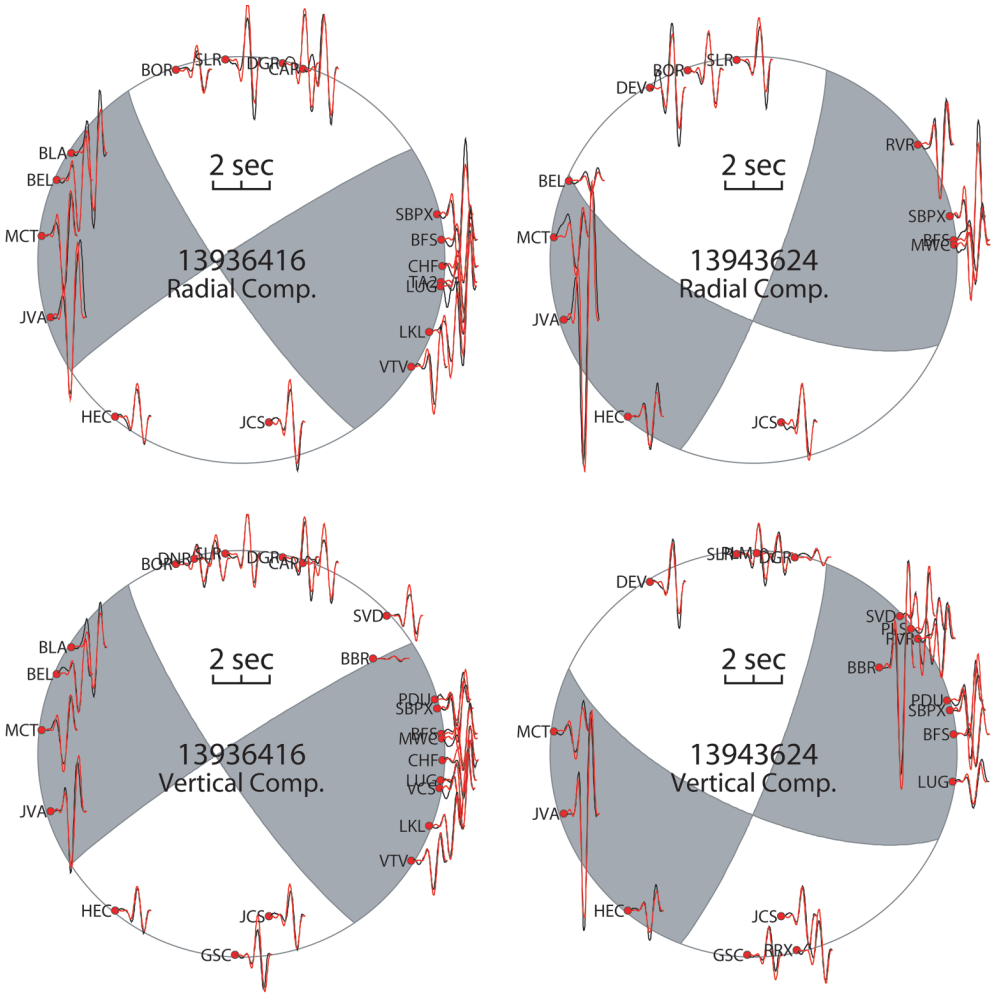

Figure 11. Comparison of *P*-wave waveform fits from the short-period inversions between the two events, 13936416 (left) and 13943624 (right), located almost at the same spot (see Fig. 10). Note the different azimuthal variations of *P*-wave amplitudes for the two events. In addition, polarity reversals are observed at a few stations, such as HEC, SVD, and BBR.

ber of events within $2.0 < M_L < 3.5$ fit well in the magnitude gap of the Ben-Zion and Zhu (2002) data. Our moment estimates of these events spanning three orders of magnitude are self-consistent, in that the larger events have been used to calibrate the structural effect for the short-period inversions of the smaller ones. Moreover, the radiation pattern effect has been removed. The least-squares fit of $\log(M_0) = 1.12\,M_L + 17.29$ explains all the data points (black symbols) except for only a few outliers (Fig. 12a). Some of the outliers also appear to have the highest stress drops, as discussed in a forthcoming article (Tan and Helmberger, manuscript in preparation). The slope of 1.12 agrees with the previous results of Bakun (1984), Vidal and Mungúia (1991), Kim *et al.* (1989), and Bindi *et al.* (2001) for events of similar size. However, we do not observe the continuous $\log(M_0)$ versus M_L curvature as suggested by Hanks and Boore (1984). We group the events according to their different fault types according to Frohlich (1992) and find no obvious dependence on fault types of the $\log(M_0) - M_L$ relation. For comparison, we include 159 events in Fig. 12b with $M_L > 3.5$ throughout southern California between 1999 and 2004 (color-coded symbols). The seismic moments of these events are determined by inverting long-period complete seismograms (Tan, 2006). The linear least-squares fit for these events gives a similar slope of 1.13, although the scatter is apparently larger, which is probably due to the regional variations of the $\log(M_0)$ versus M_L relationship, as reported by Clinton *et al.* (2006). The slope of 1.13 is smaller than the result of Ben-Zion and Zhu (2002), but it is in agreement with the result of Clinton *et al.* (2006). We group the events according to their depths, and no obvious depth dependence of the $\log(M_0) - M_L$ relation is observed. We also perform linear least-squares fit for the 31 events with $M_L > 4.5$ and obtain a significantly larger slope of 1.57, which suggests a sharp change in the scaling between $\log(M_0)$ and M_L near $M_L \sim 4.5$.

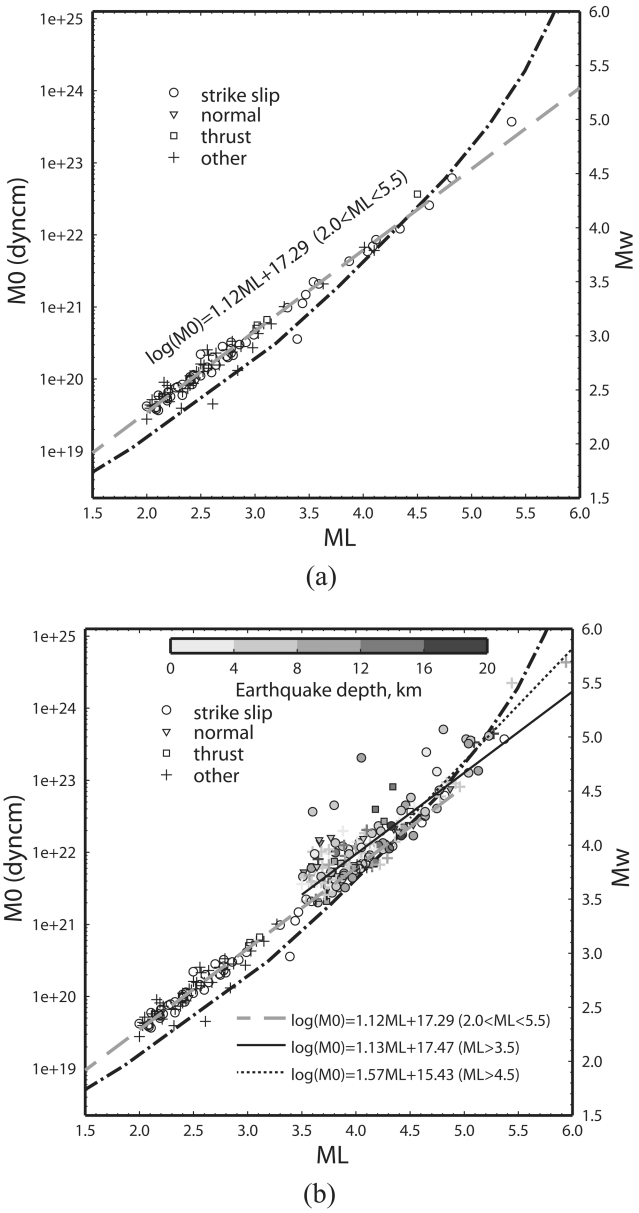

Figure 12. The M_0 versus M_L relationship for the 92 events in Figure 10, together with the linear least-squares fit (dashed line), is displayed in (a), where the events are grouped into different fault types according to Frohlich (1992). The dot-dashed line is from Hanks and Boore (1984) based on their stochastic simulations of high-frequency ground motions (Boore, 1983). About 160 events (M >3.5) color coded in depth throughout southern California since 1999 are added in (b), whose source parameters are determined from long-period inversions (Tan, 2006). The linear least-squares fits for these events and the M >4.5 subset are displayed as the solid and dotted black lines, respectively.

Discussion and Conclusion

As demonstrated earlier, *P*-wave amplitude corrections play a key role in recovering reliable source mechanisms from short-period (0.5–2 Hz) *P*-wave inversions. The use of the constant AAFs for the whole 2003 Big Bear sequence proves effective, in that large misfit error reduction has been achieved for nearly all the events. By definition, the AAFs contain the effects from the station site, the path, and crustal scattering. Isolating their contributions is difficult, especially with a single cluster. However, we can examine neighboring events outside the Big Bear sequence to better understand the spatial validity range of the AAFs. Moreover, by studying clusters at larger separations, we are able to assess the applicability of the approach to other seismic zones of interest. This also allows us to establish the controlling factors in the AAFs, as more source-specific AAFs are archived. Another issue with the AAFs is their frequency dependence, in particular, the extension to higher frequencies, for example, 2–8 Hz. In this section, we will briefly address these issues although in-depth investigations are planned for a future study.

To investigate the spatial validation range of the AAFs, we study several events with known source mechanisms from other clusters in the Big Bear vicinity. In particular, we compare the AAFs derived from these events with those from the 2003 sequence (Fig. 6). The comparison results for the two events that are the farthest (~10 km) from the 2003 sequence are displayed in Figure 13. Although there is some scatter, the AAFs from the two events agree with those from the 2003 sequence. In fact, such good agreements are observed for all the events examined, which indicates that the AAFs derived for the compact 2003 sequence are practically valid over a much larger area (~10 km by 10 km) and can be directly used to study these neighboring sequences.

The mechanism independence and stability of the AAFs (Fig. 6) suggest that they are mainly controlled by the near-receiver structure. The near-source scatters, on the contrary, would produce energy independent of the earthquake source mechanism, hence cause the AAFs to be mechanism dependent (e.g., Ebel, 1989). That is to say, the near-source scattering is not strong enough to obscure the 0.5–2 Hz *P*-wave radiation pattern. To test whether this is a coincidence at Big Bear or typical of southern California, we have conducted AAF calibration process for other source regions, in particular, of Northridge and Landers. These are the areas with more complicated geological structures, where we might expect more scattering as well. An example of the calibration results for a cluster in southern Landers is displayed in Figure 14. The detailed source parameters of the eight events used for AAF calibration were obtained by inverting long-period (>5 sec) three-component complete seismograms (Tan, 2006) and listed in Table 1. We calculate the averages and deviations of the AAFs derived from the calibration events, and only those stations with at least three AAF estimates associated with cross-correlation coefficients greater

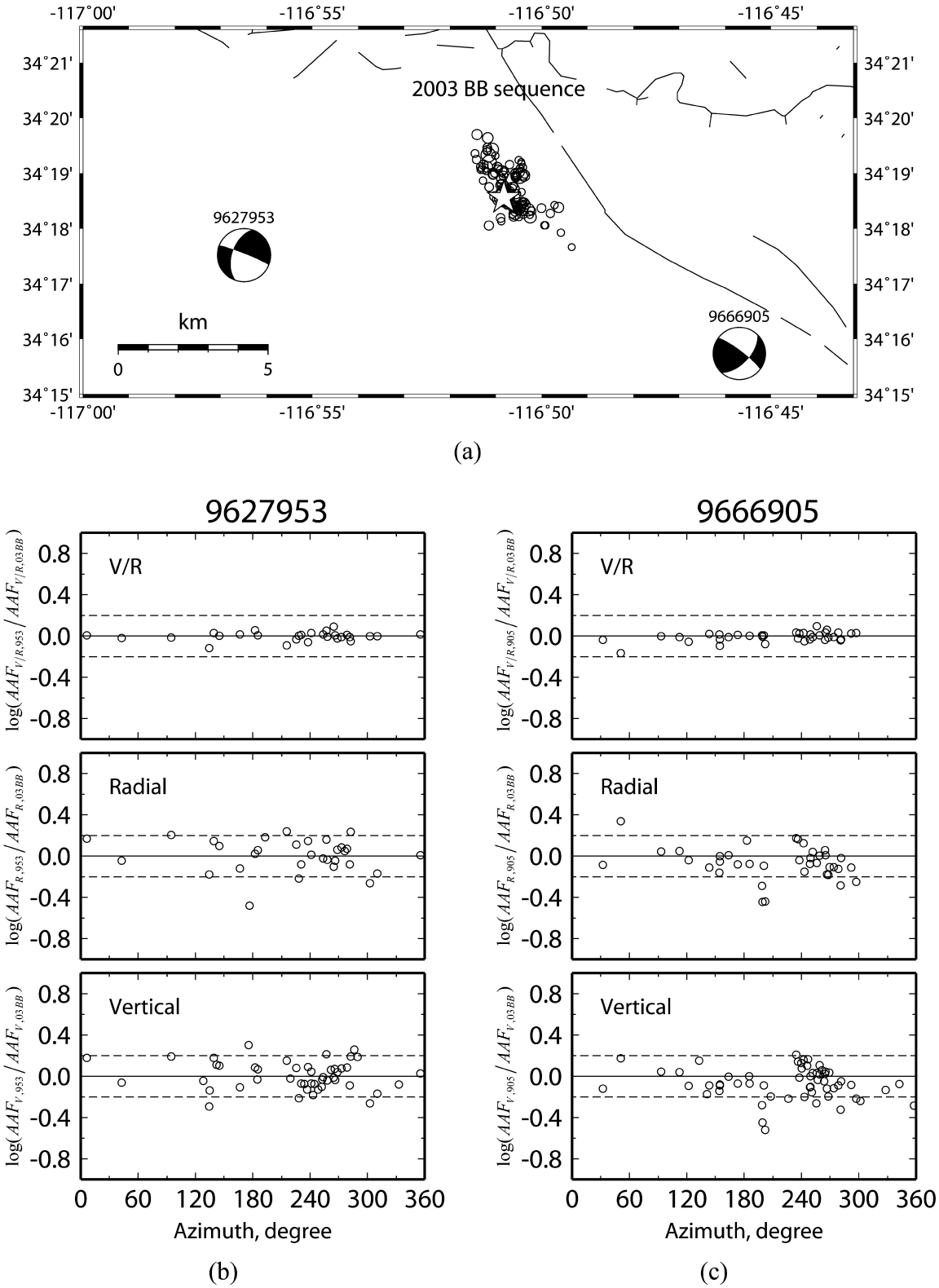

Figure 13. The source mechanisms of two past events, 9627953 (2001/02/11,00:39:15.97) and 9666905 (2001/07/03,11:40:48.11), in the Big Bear vicinity (a), together with the comparisons in (b) and (c) between the AAFs derived from them and the 2003 Big Bear sequence (Fig. 6). Only the stations that have AAF estimates from the two events associated with waveform cross-correlation between data and synthetics greater than 90 are shown.

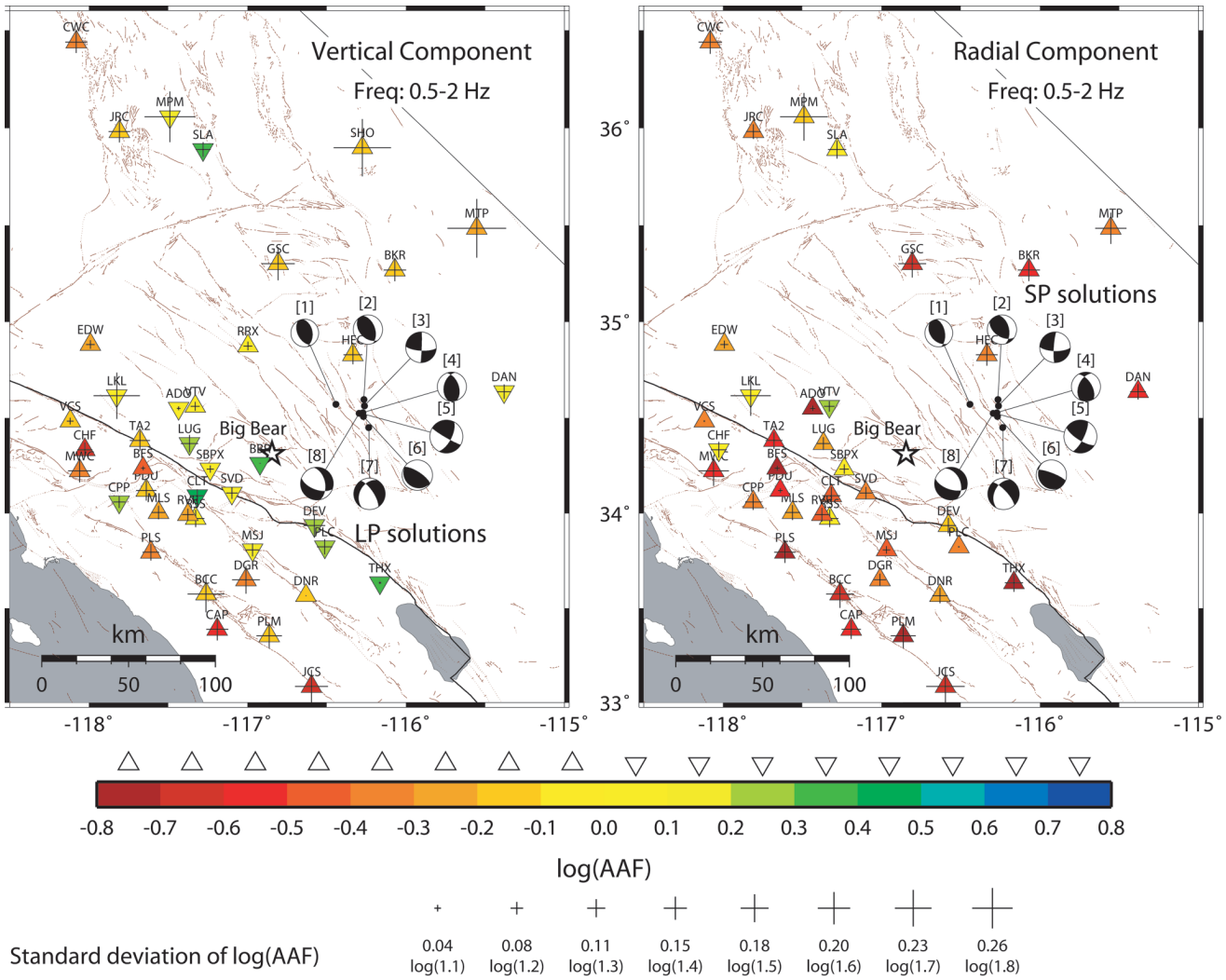

Figure 14. The averaged AAFs for the vertical (left) and radial (right) components derived from the eight calibration events in southern Landers along with the standard deviations. The open star denotes the 2003 Big Bear mainshock for reference. The long-period (LP, >5 sec) source mechanisms of the events determined by inverting complete seismograms are shown in the left, and their mechanisms obtained by inverting short-period (SP, 0.5–2 Hz) *P* waves with AAF corrections are given in the right for comparison.

than 90 are shown. Except for a few stations, such as MPM, SHO, and MTP, where the AAF estimates are controlled by the observations near the *P*-wave nodes, all the stations display stable and mechanism-independent AAFs. Among them, larger deviations are observed for the few stations (e.g., BCC, DGR, JCS, PLM) at crossover distances of upgoing and downgoing waves. Simply using the stations with stable AAFs ($s_{\log(AAF)} < 0.20$) in Figure 14, we nicely recovered the known source mechanisms of the calibration events with short-period *P*-wave inversions as displayed in Figure 14 (right side). Similar results are obtained for northern Landers and Northridge clusters, which demonstrates the usefulness of these simple corrections. Thus, it appears that the greatest barrier to modeling at short periods (<2 sec) or wavelengths less than 10 km is simply the scattering produced by the surface. This is no surprise to those researchers working with downhole arrays, but it is surprising how well simple calibration works to correct for some of these complicated features. Although not discussed here, one of the greatest advantages of working with wavelengths less than a few kilometers is that directivity effects are relatively obvious. This subject will be addressed in a subsequent article (Tan and Helmberger, manuscript in preparation), where the rupture properties of the 2003 Big Bear sequence will be investigated, displaying the large difference between events rupturing along the mainfault versus cross orientations.

In contrast to the AAFs in Figure 6, differences are observed at nearly all the stations in Figure 14, which strongly

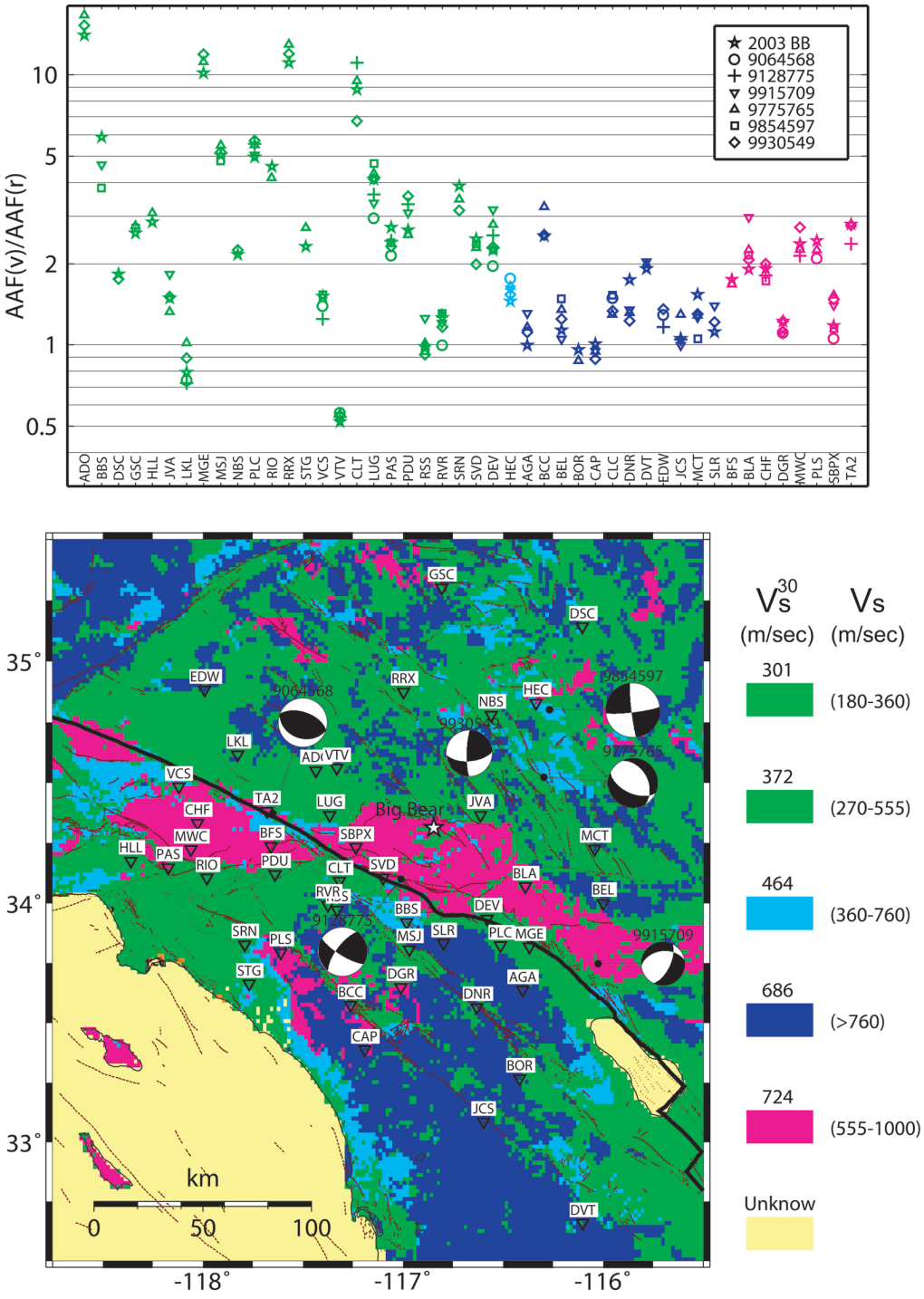

Figure 15. (top) The comparison of the ratios between the AAFs for the vertical and radial components from six events versus those from the 2003 Big Bear sequence. The stations are grouped and color coded according to their site conditions as shown in the bottom. (bottom) The source parameters of the events for comparison (from Tan, 2006) and the station locations are displayed on a geologically determined site-condition map from Wills *et al.* (2000). Labeled is the representative V_s^{30} of the top 30 m for each category, and the expected range of V_s.

Table 1
Source Parameters of Eight Events in Southern Landers from Tan (2006)

	SCSN			Fault Parameters		
Event	Event ID	Origin Date/Time	Lat/Lon	FM: $\phi/\delta/\lambda$	h	M_w
1	9805021	2002/07/31 08:31:47.980	34.57/−116.44	151/48/76	7.2	3.51
2	3324595	1999/10/22 11:34:23.653	34.60/−116.27	340/50/105	4.4	3.70
3	9114515	1999/10/22 01:58:43.078	34.56/−116.26	93/72/3	5.0	3.85
4	9114042	1999/10/21 05:47:38.865	34.53/−116.27	339/52/66	6.6	3.66
5	9117942	1999/10/29 12:36:37.514	34.52/−116.27	120/84/25	3.5	4.18
6	9114563	1999/10/22 03:49:33.489	34.51/−116.27	123/18/90	5.8	3.83
7	9108964	1999/10/16 13:51:17.620	34.45/−116.23	210/38/−32	6.3	3.96
8	9775765	2002/04/05 08:02:56.050	34.52/−116.29	349/49/−42	4.9	4.12

suggests path effects on the AAFs. Although the AAFs themselves are backazimuth and distance dependent, their ratios between the vertical and radial components appear constant and are possibly simple functions of site conditions (Fig. 15). Note the clustering of the AAF(v)/AAF(r) ratios at the various stations from events at different locations. There is also a good correlation between the AAF(v)/AAF(r) ratios and the surface geology (Fig. 15), although numerically investigating the relationship between the AAF(v)/AAF(r) ratio and the site condition will be pursued in a future study.

We focus the short-period *P*-wave calibration and inversion on a single 0.5–2 Hz band; however, as suggested in Figure 1, the same strategy can be carried to a higher-frequency band, for example, 2–8 Hz, and hence be applied to even smaller events. To examine the AAFs at higher frequencies and their usefulness in determining source mechanisms of smaller events, we conducted an AAF calibration process at 2–8 Hz with 21 M_w ~2.5 events in Figure 10. Although the deviations in general are larger, the AAFs of most stations still appear stable and mechanism independent (Fig. 16a). In fact, many of the large deviations ($s_{\log(AAF)} > 0.2$) are due to the AAF estimates near the *P*-wave nodes. More importantly, when we conducted *P*-wave inversions with these AAF corrections for the calibration events, the resulting mechanisms agree with those determined at 0.5–2 Hz shown in Figure 10. A few examples of the resultant waveform fits are given in Figure 16b. Note the nodal behavior of the few stations, such as NBS, HEC, BEL, BLA, RVR, and SVD. This preliminary study suggests that the *P*-wave radiation pattern is still preserved for a large number of stations at 2–8 Hz. As the AAFs for these stations are calibrated, they can be used for studying source mechanisms of magnitude 1 events.

In conclusion, we have developed a new technique of inverting short-period *P* waves for determining small earthquake ($M < 3.5$) focal mechanisms and moments. To account for the unmodeled structural effect, the so-called amplitude amplification factors (AAFs) are utilized in the inversions, which can be established from nearby calibration events with known source mechanisms. We have introduced the method with the application to the 2003 Big Bear sequence. However, it applies equally well to other source regions in southern California, because we have shown that the mechanism independence and stability of the AAFs for source regions of 10 km by 10 km are typical. The AAFs contain the contributions from the path, the station site, and possibly crustal scattering. To numerically investigate the origin of the AAFs is beyond the scope of this article, although the ratio between the AAFs for the vertical and radial components proves a good indicator of site conditions. Because the whole short-period calibration and inversion process is very efficient as to the current procedure and program setup, we expect to better understand the AAFs as the distance and backazimuth dependence of the AAFs for numerous stations become known.

Acknowledgments

We would like to thank Hiroo Kanamori, Egill Hauksson, Lupei Zhu, and Alex Song for useful discussions. The comments from Po Chen, Jeanne Hardebeck, and an anonymous reviewer helped to improve the manuscript. This work is supported by SCEC (USC.SCEC02), USGS (06HQGR0140), and DoE (DE-FC52-06NA27319). Caltech Seismological Laboratory contribution no. 9167.

References

Abercrombie, R. E. (1995). Earthquake source scaling relationships from −1 to 5 m_l using seismgrams recorded at 2.5-km depth, *J. Geophys. Res.* **100,** no. B12, 24,015–24,036.

Atkinson, G. M., and S. E. McCartney (2005). A revised magnitude-recurrence relation for shallow crustal earthquakes in Southwestern British Columbia: considering the relationships between moment magnitude and regional magnitudes, *Bull. Seism. Soc. Am.* **95,** no. 1, 334–340.

Bakun, W. H. (1984). Seismic moments, local magnitudes, and coda-duration magnitudes for earthquakes in central California, *Bull. Seism. Soc. Am.* **74,** no. 2, 439–458.

Ben-Zion, Y., and J. R. Rice (1993). Earthquake failure sequences along a cellular fault zone in a three-dimensional elastic solid containing asperity and nonasperity regions, *J. Geophys. Res.* **98,** 14,109–14,131.

Ben-Zion, Y., and L. Zhu (2002). Potency-magnitude scaling relations for southern California earthquakes with $1.0 < m_l < 7.0$, *Geophys. J. Int.* **148,** F1–F5.

Beroza, G. C., and M. D. Zoback (1993). Mechanism diversity of the Loma Prieta aftershocks and the mechanics of mainshock-aftershock interaction, *Science* **259,** 210–213.

Bindi, D., D. Spallarossa, P. Augliera, and M. Cattaneo (2001). Source parameters estimated from the aftershocks of the 1997 Umbria-Marche (Italy) seismic sequence, *Bull. Seism. Soc. Am.* **91,** no. 3, 3448–3455.

Boore, D. M. (1983). Stochastic simulation of high-frequency ground motions based on seismological models of the radiated spectra, *Bull. Seism. Soc. Am.* **73,** no. 6, 1865–1894.

Braunmiller, J., N. Deichmann, D. Giardini, and S. Wiemer (2005). Homogeneous moment-magnitude calibration in Switzerland, *Bull. Seism. Soc. Am.* **95,** no. 1, 58–74.

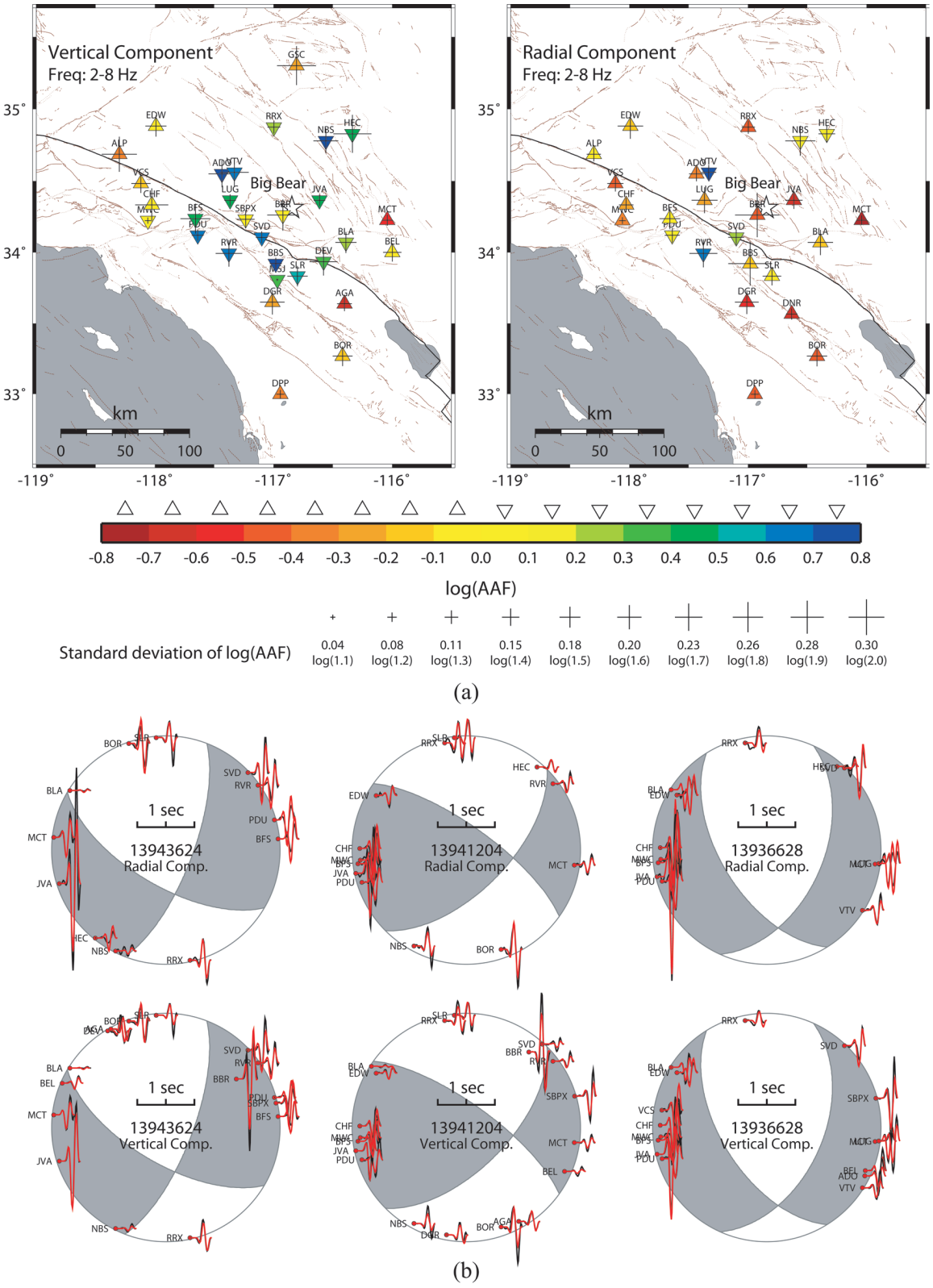

Figure 16. (a) The averaged AAFs along with the standard deviations for the vertical (left) and radial (right) components derived from 21 magnitude ~2.5 events in Figure 10 at 2–8 Hz. (b) Comparison of *P*-wave waveform fits from short-period inversions at 2–8 Hz of three events with different mechanisms.

Chen, P., T. H. Jordan, and L. Zhao (2005). Finite-moment tensor of the 3 September 2002 Yorba Linda earthquake, *Bull. Seism. Soc. Am.* **95,** no. 3, 1170–1180.

Chi, W.-C., and E. Hauksson (2006). Fault-perpendicular seismicity after 2003 Mw = 4.9 Big Bear, California earthquake: implications for static stress triggering, *Geophys. Res. Lett.* **33,** L07301, doi 10.1029/2005GL025,033.

Clinton, J. F., E. Hauksson, and K. Solanki (2006). Automatically generated moment tensor solutions for southern California: robustness of the m_w magnitude scale and style of faulting, *Bull. Seism. Soc. Am.* **96,** no. 5, 1689–1705.

Deichmann, N. (2006). Local magnitude, a moment revisited, *Bull. Seism. Soc. Am.* **96,** no. 4A, 1267–1277.

Dreger, D., and D. V. Helmberger (1993). Determination of source parameters at regional distances with three-component sparse network data, *J. Geophys. Res.* **98,** no. B5, 8107–8125.

Ebel, J. E. (1989). The effect of crustal scattering on observed high-frequency earthquake seismograms, *Geophys. J. Int.* **98,** 329–341.

Ebel, J. E., and K. P. Bonjer (1990). Moment tensor inversion of small earthquakes in southwestern Germany for the fault plane solution, *Geophys. J. Int.* **101,** 133–146.

Frohlich, C. (1992). Triangle diagrams: ternary graphs to display similarity and diversity of earthquake focal mechanisms, *Phys. Earth Planet. Interiors* **75,** 193–198.

Hanks, T. C., and D. M. Boore (1984). Moment-magnitude relations in theory and practice, *J. Geophys. Res.* **89,** no. B7, 6229–6235.

Hardebeck, J. L., and E. Hauksson (1997). Static stress drop in the 1994 Northridge, California, aftershock sequence, *Bull. Seism. Soc. Am.* **87,** no. 6, 1495–1501.

Hardebeck, J. L., and E. Hauksson (2001). Crustal stress field in southern California and its implications for fault mechanics, *J. Geophys. Res.* **106,** no. B10, 21,859–21,882.

Hardebeck, J. L., and P. M. Shearer (2002). A new method for determining first-motion focal mechanisms, *Bull. Seism. Soc. Am.* **92,** no. 6, 2264–2276.

Hardebeck, J. L., and P. M. Shearer (2003). Using S/P amplitude ratios to constrain the focal mechanisms of small earthquakes, *Bull. Seism. Soc. Am.* **93,** no. 6, 2434–2444.

Hauksson, E. (1994). State of stress from focal mechanisms before and after the 1992 Landers earthquake sequence, *Bull. Seism. Soc. Am.* **84,** no. 3, 917–934.

Hauksson, E., L. M. Jones, K. Hutton, and D. Eberhart-Phillips (1993). The 1992 Landers earthquake sequence: Seismological observations, *J. Geophys. Res.* **98,** no. B11, 19,835–19,858.

Helmberger, D. V. (1983). Theory and application of synthetic seismograms, in *Earthquakes: Observation, Theory and Interpretation*, Soc. Italiana di Fisica, Bolgna, Italy, 174-222.

Julian, B. R., and G. R. Foulger (1996). Earthquake mechanisms from linear-programming inversion of seismic-wave amplitude ratios, *Bull. Seism. Soc. Am.* **86,** no. 4, 972–980.

Kilb, D., M. Ellis, J. Gomberg, and S. Davis (1997). On the origin of diverse aftershock mechanisms following the 1989 Loma Prieta earthquake, *Geophys. J. Int.* **128,** 557–570.

Kim, W.-Y., R. Wahlström, and M. Uski (1989). Regional spectral scaling relations of source parameters for earthquakes in the Baltic Shield, *Tectonophysics* **166,** 151–161.

Kisslinger, C. (1980). Evaluation of *s* to *p* amplitude ratios for determining focal mechanisms from regional network observations, *Bull. Seism. Soc. Am.* **70,** no. 4, 999–1014.

Koch, K. (1991a). Moment tensor inversion of local earthquake data. I. Investigation of the method and its numerical stability with model calculations, *Geophys. J. Int.* **106,** 305–319.

Koch, K. (1991b). Moment tensor inversion of local earthquake data. II. Application to aftershocks of the May 1980 Mammmoth Lakes earthquakes, *Geophys. J. Int.* **106,** 321–332.

Liu, Q., J. Polet, D. Komatitsch, and J. Tromp (2004). Spectral-element moment tensor inversions for earthquakes in southern California, *Bull. Seism. Soc. Am.* **94,** no. 5, 1748–1761.

Nakamura, A., S. Horiuchi, and A. Hasegawa (1999). Joint focal mechanism determination with source–region station corrections using short-period body-wave amplitude data, *Bull. Seism. Soc. Am.* **89,** no. 2, 373–383.

Natale, G. D., A. Ferraro, and J. Virieux (1991). A probability method for local earthquake focal mechanisms, *Geophys. Res. Lett.* **18,** no. 4, 613–616.

Rau, R.-J., F. T. Wu, and T.-C. Shin (1996). Regional network focal mechanism determination using 3D velocity model and *sh/p* amplitude ratio, *Bull. Seism. Soc. Am.* **86,** no. 5, 1270–1283.

Reasenberg, P., and D. Oppenheimer (1985). FPFIT, FPPLOT, and FPPAGE: FORTRAN computer programs for calculating and displaying earthquake fault-plane solutions, in *U.S. Geol. Surv. Open-File Rept. 85-739.*

Saikia, C. K., and R. B. Herrmann (1985). Application of waveform modeling to determine focal mechanisms of four 1982 Miramichi aftershocks, *Bull. Seism. Soc. Am.* **75,** no. 4, 1021–1040.

Saikia, C. K., and R. B. Herrmann (1986). Moment-tensor solutions for three 1982 Arkansas swarm earthquakes by waveform modeling, *Bull. Seism. Soc. Am.* **76,** no. 3, 709–723.

Savage, B., and D. V. Helmberger (2004). Site response from incident *pnl* waves, *Bull. Seism. Soc. Am.* **94,** no. 1, 357–362.

Schurr, B., and J. Nábělek (1999). New techniques for the analysis of earthquake sources from local array data with an application to the 1993 Scotts Mills. Oregon aftershock sequence, *Geophys. J. Int.* **137,** 585–600.

Schwartz, S. Y. (1995). Source parameters of aftershocks of the 1991 Costa Rica and 1992 Cape Mendocino, California, earthquakes from inversion of local amplitude ratios and broadband waveforms, *Bull. Seism. Soc. Am.* **85,** no. 6, 1560–1575.

Shearer, P. M. (1998). Evidence from a cluster of small earthquakes for a fault at 18 km depth beneath Oak Ridge, southern California, *Bull. Seism. Soc. Am.* **88,** 1327–1336.

Sileny, J., G. F. Panza, and P. Campus (1992). Waveform inversion for point source moment tensor retrieval with variable hypocentral depth and structural model, *Geophys. J. Int.* **109,** 259–274.

Song, X. J., and D. V. Helmberger (1998). Pseudo Green's functions and waveform tomography, *Bull. Seism. Soc. Am.* **88,** no. 1, 304–312.

Tan, Y. (2006). Broadband waveform modeling over a dense seismic network, *Ph.D. Thesis*, California Institute of Technology, Pasadena, California.

Tan, Y., L. Zhu, D. V. Helmberger, and C. K. Saikia (2006). Locating and modeling regional earthquakes with two stations, *J. Geophys. Res.* **111,** B01306, doi 10.1029/2005JB003,775.

Thio, H.-K., and H. Kanamori (1995). Moment-tensor inversion for local earthquakes using surface waves recorded at TERRAscope, *Bull. Seism. Soc. Am.* **85,** 1021–1038.

Vidal, A., and L. Mungúia (1991). Local magnitude and source parameters for earthquakes in the Peninsular Ranges of Baja California, Mexico, *Bull. Seism. Soc. Am.* **81,** no. 6, 2254–2267.

Wills, C. J., M. Petersen, W. A. Bryant, M. Reichle, G. J. Saucedo, S. Tan, G. Taylor, and J. Treiman (2000). A site-conditions map for California based on geology and shear-wave velocity, *Bull. Seism. Soc. Am.* **90,** no. 6B, S187–S208.

Zhao, L. S., and D. V. Helmberger (1994). Source estimation from broadband regional seismograms, *Bull. Seism. Soc. Am.* **84,** 91–104.

Zhu, L., and D. V. Helmberger (1996). Advancement in source estimation techniques using broadband regional seismograms, *Bull. Seism. Soc. Am.* **86,** 1634–1641.

Zhu, L., and L. A. Rivera (2002). A note on the dynamic dand static displacements from a point source in multi-layered media, *Geophys. J. Int.* **148,** 619–627.

Appendix A

Are the AAFs Stable and Mechanism Independent?

Figure A1 displays the comparison between the AAFs derived from the strike-slip event 13938812) and the distinctly different thrust event (13936812). Although there is some scatter, the ratios between the AAFs at the same stations tend to follow a straight line, which supports the argument that the AAFs are stable and independent of the source mechanism. Note that the scatter becomes slightly larger near the *P*-wave nodes of the events, where the few obvious outliers occur. Potential sources of the scatter include small errors in the events locations, source mechanisms, the rupture complexities, as well as small-scale structural heterogeneity. The small offset of ~ -0.15 in $\log(AAF_{6812}/AAF_{8812})$ implies that the AAFs derived from the thrust event (13936812) are consistently smaller than those from the strike-slip event (13938812) by a factor of $\sim$30%, which suggests that the thrust event might have relatively longer, but lower-amplitude source time function. Experiments indicate that the observed offset in $\log(AAF_{6812}/AAF_{8812})$ can be reconciled by simply assuming a 0.4-sec triangular source time function in constructing the synthetics for the thrust event. The longer source duration also fits the observations slightly better. This underlines the importance of understanding seismic-source complexities in calibrating the structural effect. However, because fairly good agreements without significant offsets are observed when we compare the AAFs derived from the other calibration events with those from the strike-slip event 13938812, the simple triangular source time function of 0.2 sec might present a safe approximation in the selected 0.5–2 sec frequency band. In particular, for the calculations displayed in Figure 6, the AAFs derived from the thrust event (13936812) have been corrected with the ~ -0.15 offset in $\log(AAF_{6812}/AAF_{8812})$ with respect to the rest of the events. However, the correction hardly made a difference, simply because the offset itself is not significant compared with the scatter in the AAFs.

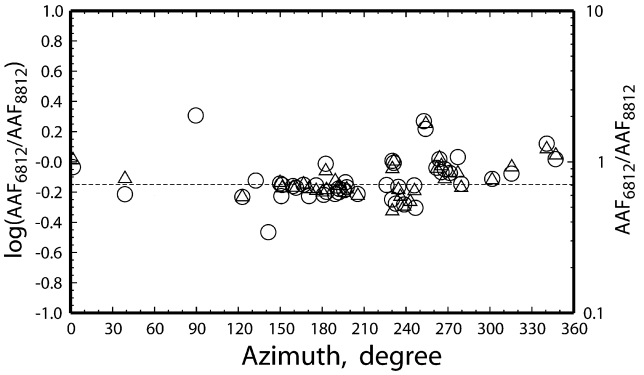

Figure A1. Comparison of the AAFs derived from the strike-slip event (13938812) and the thrust event (13936812) for the same stations. Shown are their log $\log(AAF_{6812}/AAF_{8812})$ and linear AAF_{6812}/AAF_{8812} ratios versus azimuth. The circles are for the vertical component and the triangles are for the radial.

Seismological Laboratory, 252-21
California Institute of Technology
Pasadena, California

Manuscript received 6 December 2006.